GENERATING LOW BETA REGIONS WITH QUADRUPOLES FOR FINAL MUON COOLING*

J. G. Acosta†, L. M. Cremaldi, T. L. Hart, S. J. Oliveros, and D. J. Summers
University of Mississippi - Oxford, University, MS 38677 USA
D. V. Neuffer, Fermilab, Batavia, IL 60510 USA

Abstract

Muon beams and colliders are rich sources of new physics, if muons can be cooled. A normalized rms transverse muon emittance of 280 microns has been achieved in simulation with short solenoids and a betatron function of 3 cm. Here we use ICOOL, G4beamline, and MAD-X to explore using a 400 MeV/c muon beam and strong focusing quadrupoles to approach a normalized transverse emittance of 100 microns and finish 6D muon cooling. The low beta regions produced by the quadrupoles are occupied by dense, low Z absorbers, such as lithium hydride or beryllium, that cool the beam. Equilibrium transverse emittance is linearly proportional to the beta function. Reverse emittance exchange with septa and/or wedges is then used to decrease transverse emittance from 100 to 25 microns at the expense of longitudinal emittance for a high energy lepton collider. Work remains to be done on chromaticity correction.

INTRODUCTION

Ionization cooling is fast enough to cool muons and is being tested at the MICE [1–13] experiment. The basic theory of transverse and longitudinal cooling is described in [14]. Two cooling schemes [15, 16] have been proposed to reduce muon emitances for a lepton collider [17–51]. Simulation results are shown in Table 1.

Table 1: Helical and Rectilinear Cooling Channel normalized 6D emittances ϵ_{6D} from simulations and the emittances needed for a muon collider. The channels cool by over five orders of magnitude and need less than a factor of 10 more for a collider. The 21 bunches present after initial phase rotation are also merged into one bunch during cooling [52].

	ϵ_x mm	ϵ_y mm	ϵ_y mm	ϵ_{6D} mm^3
Initial Emittance [15]	48.6	48.6	17.0	40,200
Helical Cooling [16]	0.523	0.523	1.54	0.421
Rectilinear Cooling [15]	0.28	0.28	1.57	0.123
Muon Collider [53]	0.025	0.025	70	0.044

For a given magnetic field, quadrupole focusing can achieve lower betatron functions than solenoids to reduce the equilibrium emittances below those shown in Table 1.

* supported by Fermi Research Alliance, LLC under Contract No. DE-AC02-07CH11359 with the U. S. Department of Energy
† johnacos@phy.olemiss.edu

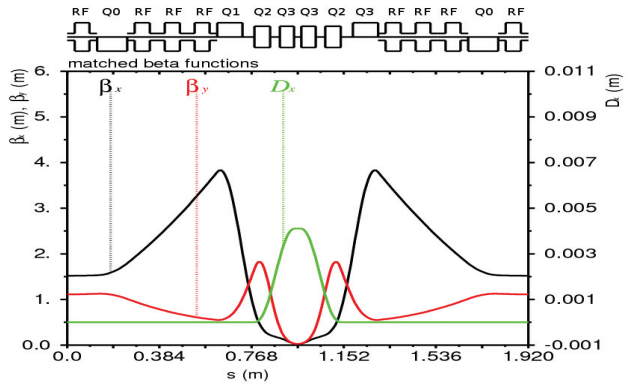

Figure 1: Betatron functions [54, 55] and dispersion vs. distance s, as determined by MAD -X.

CHANNEL DESIGN

Low equilibrium emittance requires low $< \beta_\perp >$. Strong quadrupole focusing [56, 57] can achieve $\beta^*_\perp$ values within the required 0.5 to 2.0 cm range. A half cell is composed of four quadrupole magnets: the magnet (Q0) is a coupling quadrupole preceded by an RF (radio frequency) cavity (L=0.125 m) and separated by three following RF (L=0.125 m) cavities. The 650 MHz RF has a phase angle 11.5° away from zero crossing and a 27.87 MV/m gradient. The following quadrupole magnets (Q2, Q3) are separated by a short drift space to avoid excessive fringe field interference [58] between magnets, as shown in Fig. 1.

The bore diameter and length for the first quadrupole magnet Q0 is 12.5 cm. The Q0 magnet works as a coupling quadrupole reducing the betatron function maximum and allows the addition of more RF cavities to increase longitudinal synchrotron focusing. The bore diameter and length for the second quadrupole (Q1) is 10.5 cm followed by a Q2 magnet with length and diameter of 6.5 cm. A 6.0 cm long central quadrupole Q3 with 3 cm bore radius is added to reduce both the chromaticity and the minimum betatron function. The 192 cm long full cell has a 3 cm drift space for an absorber shown in Fig. 2. The quadrupoles Q2 and

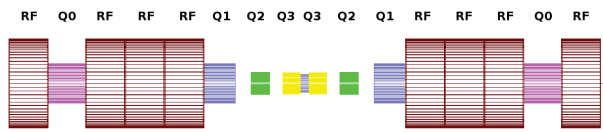

Figure 2: G4beamline full cell.

ISBN 978-3-95450-182-3

Q3 have a dipole magnetic component to produce a uniform dispersion of 4.1 mm at the absorber [59–61].

This configuration provides strong focusing using magnetic pole tip fields of Q0 = 0.75 T, Q1 = 4.69 T, Q2 = 9.02 T, and Q3 = 11.40 T. Quadrupoles with peak fields of more than 12 T have been built with Nb_3Sn [62,63]. The magnetic lattice has $\beta_{x,max} \cong 2\beta_{y,max}$.

Higher transmission might be achieved by increasing the momentum acceptance from that shown in Fig. 3. Off momentum muons may not focus in the LiH, may shift phase into the π or 2π stop bands, or may increase betatron functions beyond the acceptance of magnet bores. The momentum acceptance of the channel needs to be increased from 6% to 10%. The ILC corrects chromaticity with a system of two widely separated quadrupole doublets [64]. Each of the four quadrupoles has dispersion plus a sextupole. The quadrupole doublets are point to point focusing which generates a 180° phase advance between x sextupole pairs and y sextupole pairs in the low beta region between the doublets.

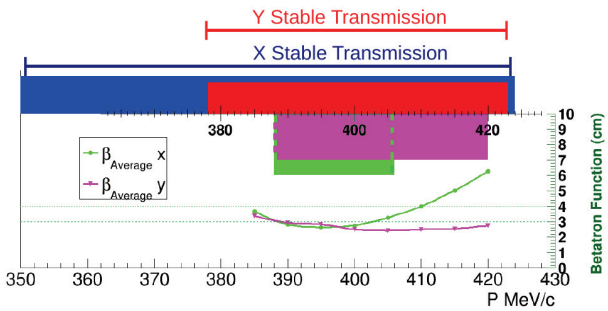

Figure 3: The blue bar is the region where the magnetic lattice has stable transmission for X. The red bar shows the stable transmission band for the Y dimension. The green and pink bars indicate that the momentum ranges where $< \beta_x >< 3$ cm and $< \beta_y >< 3$ cm are 388 < p < 402 MeV/c and 391 < p < 422 MeV/c, respectively.

MAD-X [65, 66] sets magnet parameters to constrain the phase advances per 1.92 m long full cell to $(\mu_x, \mu_y) = 2\pi\,(0.68, 0.70)$ rad. Dispersion is flat and constant at the absorber locations and zero at the cell ends. The average transverse betatron functions over the 3 cm long absorber regions is less than 3 cm for a 400 MeV/c muon.

The quadrupole triplet configuration is designed for a beam near 400 MeV/c and $(\beta_x^*, \beta_y^*) = (2.2, 2.7)$ cm at the centers of the absorbers. Momentum variations affect the longitudinal locations of β_x^* and β_y^* as Fig. 3 shows and can shift the minima outside the absorbers.

Wedge and Dispersion for Emittance Exchange

The Q2, Q3 quadrupoles have dipole magnetic field components of 0.49 T and 0.68 T calculated to create a constant η = 4.1 mm dispersion at the absorber region as Fig. 1 shows. A 105° lithium hydride wedge is placed at the center of the 1.92 m long full cell, as shown in Fig. 4. The ends of the wedge extend into the Q3 magnet bores on each side of the wedge. The wedge geometry and the dispersion magnitude modify the partition numbers [14, 67] as equation 1 shows.

$$g_L = g_{L,0} + \frac{\eta}{W}, g_x = 1 - \frac{\eta}{W} \quad (1)$$

where η is the dispersion magnitude and W the distance from wedge apex to the reference orbit. The values for η and W are chosen to reduce the equilibrium longitudinal emittance at the expense of the equilibrium x emittance. This emittance exchange prevents longitudinal beam heating and results in longitudinal and transverse beam cooling. Two consecutive cells have opposite bending directions to make a snake channel configuration.

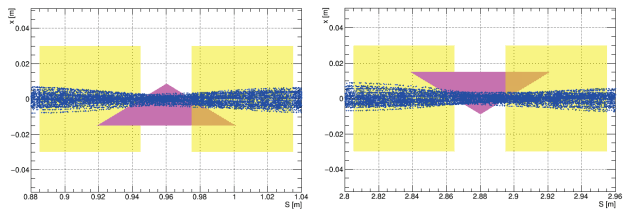

Figure 4: Wedges at the centers of the first and second cells.

FIRST STAGE SIMULATION

The first stage of the channel is simulated using G4beamline [68] and ICOOL [69, 70]. A simulation of 1000 muons with p = 400 ± 8 MeV/c through 68 full cells (total length = 130.56 m) and achieves 99% beam transmission through a lattice with no RF cavities and no absorbers. The emittance for x and y was 380 and 274 μm. When the absorbers and RF are included and the stochastic processes including decays are on, the transmission drops to 58%. Figure 5 shows transmission vs. distance. Initial beam correlations are important. Higher momentum muons should follow longer path lengths to stay in phase with the RF.

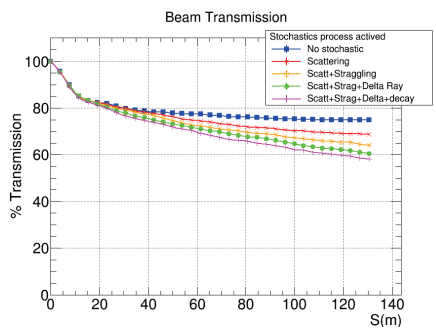

Figure 5: 58% transmission through a 130.56 meter long channel (68 full cells).

The first channel stage was simulated using ICOOL and G4beamline and had initial emittances of $\epsilon_{x,y,z}$ = (0.373, 0.236, 1.238) mm. The normalized emittances are reduced to $\epsilon_{x,y,z}$ = (0.278, 0.185, 0.960) mm as Fig. 6 shows. The total $\epsilon_{6D,N}$ emittance is reduced by 54% in the 130.56 meter long channel (Fig. 7), but this reduction is a combination of both beam loss through scraping and beam cooling.

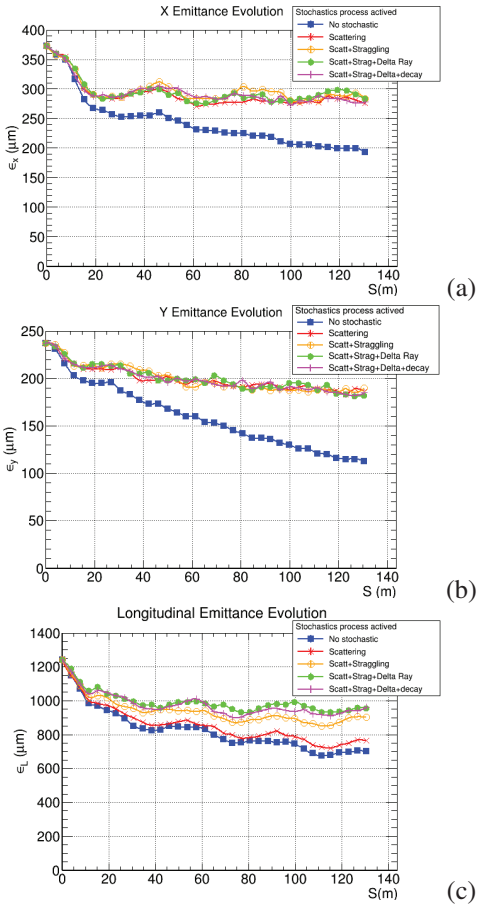

Figure 6: Emittance evolution plots. (a) ϵ_x, (b) ϵ_y and (c) ϵ_L. The initial emittance goes from $\epsilon_{x,y,z}$ = (0.373, 0.236, 1.238) to (0.278, 0.185, 0.960) mm. (Emittances are calculated using the ICOOL's eigemit tool).

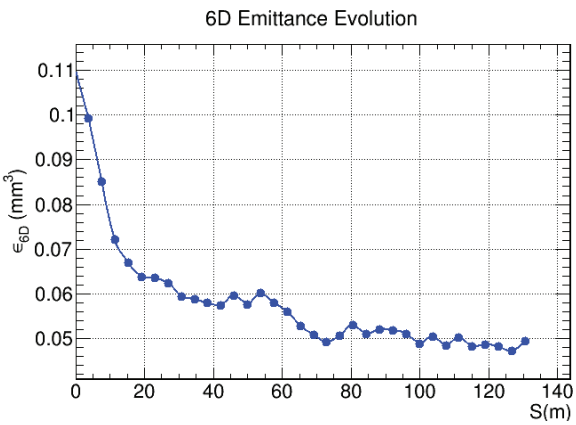

Figure 7: 6D emittance evolution. The Z-X emittance exchange prevents a natural longitudinal emittance increase.

Channel Stages

Calculations [57], but not simulations, have been done for more channel stages to complete the 6D cooling. The low $\beta^*_\perp$ regions of these additional stages are occupied by absorbers made with different low Z materials such as lithium hydride or CVD diamond. Table 3 shows why diamond is being considered. In spite of the equilibrium emittance increment of a factor of two from LiH to diamond, the energy lost per centimeter increases by a factor of four. Thus, the absorber thickness can be less with the same energy loss. If β^* is reduced enough, the transverse equilibrium emittance is reduced as well, and the desired cooling can still occur.

Table 2: First Stage Channel emittances comparison. The initial emittances are set according to the channel admittance showed by the ICOOL simulation (no RF, no absorbers). The expected emittance is calculated as $\epsilon_i(s) = (\epsilon_{0,i} - \epsilon_{i,equi}) \exp(-s\frac{g_i(dP_\mu/ds)}{P_\mu}) + \epsilon_{i,equi}$. The final ICOOL emittances are obtained from the EIGEMIT ICOOL calculator. The calculated 6D emittance reduction is 1.4× and the ICOOL simulation gives a reduction of 2.2×, which includes some scraping as well as cooling.

Emittance	ϵ_x mm	ϵ_y mm	ϵ_L mm	ϵ_{6D} mm^3
Equilibrium	0.2658	0.1460	1.4208	0.0551
Initial	0.3727	0.2367	1.2380	0.1092
Final Expected	0.3276	0.1847	1.2905	0.0781
Final ICOOL	0.2779	0.1852	0.9627	0.0496

Table 3: Material calculated equilibrium emittances. dE/ds is the energy loss at p = 400 MeV/c. The equilibrium emittances are calculated for $< \beta_\perp >$ = 2.5 cm, β_L = 40 cm, wedge angle $\alpha_w = 105°$ and $\Delta g = 0.356$.

Material	**dE/ds** MeV/cm	$\mathbf{g_{L,0}}$ $x10^{-2}$	$\boldsymbol{\epsilon}_{\mathbf{X,eq}}$ μm· rad	$\boldsymbol{\epsilon}_{\mathbf{Y,eq}}$ μm·rad	$\boldsymbol{\epsilon}_{\mathbf{L,eq}}$ μm· rad
H_2 liquid	0.288	2.004	137.8	88.75	1626
LiH	1.622	2.648	223.2	143.8	1667
Be	3.075	3.414	324.1	208.8	1714
B_4C	4.334	3.836	407.6	262.5	1739
Diamond	6.474	3.712	454.9	288.8	1732

CONCLUSION

The quadrupole channel presented shows a factor of 2.2 6D emittance reduction with 58% transmission through the first 130.56 meters stage. Scattering, straggling, delta rays, and decays were on. Some of the reduction is scraping and some cooling. More tapered stages will be required to further reduce the 6D emittance. The transmission needs to be roughly 85% per stage which will require sextupole correction of chromaticity. Reverse emittance exchange with septa [57, 71–75] and/or wedges [76] is then used to decrease transverse emittance from 100 to 25 μm at the expense of longitudinal emittance for a lepton collider.

Many thanks to Yuri Alexahin, Scott Berg, Chandra Bhat, Alex Bogacz, Yunhai Cai, Dave Cline, Mary Anne Cummings, Al Garren, Eliana Gianfelice-Wendt, Stu Henderson, Harold Kirk, Robert Palmer, Tom Roberts, Pavel Snopok, Diktys Stratakis, Alvin Tollestrup, and Glen White for help.

ISBN 978-3-95450-182-3

REFERENCES

[1] M. Bogomilov *et al.,* arXiv:1701.06403.

[2] M. Bogomilov *et al., JINST* **7** (2012) P05009.

[3] D. Adams *et al., Eur. Phys. J.* **C73** (2013) 2582.

[4] D. Adams *et al., JINST* **10** (2016) P12012.

[5] L. Cremaldi *et al., IEEE Trans. Nucl. Sci.* **56** (2009) 1475.

[6] M. Bogomilov *et al., JINST* **11** (2016) P03001.

[7] S. Ozaki *et al.,* BNL-52623 (2001).

[8] P. Franchini, IPAC-2017-WEPAB130.

[9] C. Hunt *et al.,* IPAC-2017-WAPAB131.

[10] T. Luo *et al.,* IPAC 2017-THPIK118.

[11] Tanaz Angelina Mohayai *et al.,* IPAC-2017-WEPAB135.

[12] D. Neuffer *et al.,* IPAC-2017-WEPAB133.

[13] C. T. Rogers, IPAC-2017-WEPAB129.

[14] D. Neuffer, arXiv:1312.1266.

[15] D. Stratakis and R. Palmer, *PRSTAB* **18** (2015) 031003.

[16] C. Yoshikawa *et al.,* IPAC-2014-TUPME016.

[17] J. Gallardo *et al.,* Snowmass 1996, BNL-52503.

[18] G. I. Budker, *Conf. Proc.* **C690827** (1969) 33.

[19] G. I. Budker, *AIP Conf. Proc.* **352** (1996) 5.

[20] A. N. Skrinsky, *AIP Conf. Proc.* **352** (1996) 6.

[21] D. Neuffer, Fermilab-FN-0319 (1979).

[22] A. N. Skrinsky and V. V. Parkhomchuk, *Sov. J. Part. Nucl.* **12** (1981) 223.

[23] D. Neuffer, *AIP Conf. Proc.* **156** (1987)

[24] D. Cline, *Nucl. Instrum. Meth.* **A350** (1994) 24.

[25] D. Neuffer and R. Palmer, EPAC 1994, BNL-61267.

[26] R. Palmer *et al., AIP Conf. Proc.* **372** (1996) 3.

[27] R. Palmer *et al., Nucl. Phys. Proc. Suppl.* **51A** (1996) 61.

[28] V. Barger *et al., Phys. Rept.* **286** (1997) 1.

[29] R. Raja and A. Tollestrup, *Phys. Rev.* **D58** (1998) 013005.

[30] C. M. Ankenbrandt *et al., PRSTAB* **2** (1999) 081001.

[31] K.-J. Kim and C.-X. Wang, *Phys. Rev. Lett.* **85** (2000) 760.

[32] G. Penn and J. Wurtele, *Phys. Rev. Lett.* **85** (2000) 764.

[33] M. M. Alsharo'a *et al., PRSTAB* **6** (2003) 081001.

[34] R. Palmer *et al., PRSTAB* **8** (2005) 061003.

[35] D. J. Summers *et al.,* PAC07-THPMS082.

[36] D. J. Summers *et al.,* IPAC 2012, arXiv:1207.6730.

[37] J. S. Berg and A. A. Garren, BNL-98171-2012-IR.

[38] J. C. Gallardo and M. S. Zisman, IPAC-2010-WEPE074.

[39] G. T. Lyons III, Master's Thesis, arXiv:1112.1105.

[40] D. J. Summers *et al., AIP Conf. Proc.* **1507** (2012) 860.

[41] S. A. Bogacz *et al.,* IPAC-2013-WEOAB202.

[42] J. P. Delahaye *et al.,* arXiv:1308.0494.

[43] D. Stratakis *et al., PRSTAB* **16** (2013) 091001.

[44] M. Chung *et al., Phys. Rev. Lett.* **111** (2013) 184802.

[45] B. Freemire *et al., Phys. Rev. Accel. Beams* **19** (2016) 062004.

[46] M.-H. Wang *et al., JINST* **11** (2016) P09003.

[47] T. Hart *et al.,* IPAC-2016-TUPOB44.

[48] J. G. Acosta, Ph.D. Dissertation, Univ. of Mississippi (2017).

[49] D. Neuffer *et al.,* IPAC-2016-TUPOB06.

[50] D. V. Neuffer *et al.,* IPAC-2017-TUPIK038.

[51] D. Stratakis, "A hybrid six-dimensional muon cooling channel using gas filled rf cavities," *JINST* (2017).

[52] Y. Bao *et al., Phys. Rev. Accel. Beams* **19** (2016) 031001.

[53] R. B. Palmer *et al.,* PAC 2007, arXiv:0711.4275.

[54] E. D. Courant and H. S. Snyder, *Annals Phys.* **3** (1958) 1.

[55] M. Sands, SLAC-R-121 (1970).

[56] S. Feher and J. Strait, Snowmass-1996-ACC042.

[57] D. J. Summers *et al.,* IPAC-2015-TUPWI044.

[58] C. Johnstone, M. Berz, D. Errede, and K. Makino, Fig. 5 on page 479, *Nucl. Instrum. Meth.* **A519** (2004) 472.

[59] Al Garren and Harold Kirk, MAP-DOC-4408 (2002).

[60] H. Kirk *et al., Conf. Proc.* **C030512** (2003) 2008.

[61] A. Garren *et al., AIP Conf. Proc.* **821** (2006) 415.

[62] F. Borgnolutti *et al., IEEE Trans. Appl. Supercond.* **24** (2014) 4003005.

[63] P. Ferracin *et al., IEEE Trans. Appl. Supercond.* **24** (2014) 4002306.

[64] P. Raimondi and A. Seryl, *Phys. Rev. Lett.* **86** (2001) 3779.

[65] Hans Grote *et al.,* "MAD-X Methodical Accelerator Design Version 5.02.08 User's Reference Manual," (2016).

[66] W. Herr and F. Schmidt, CERN-AB-2004-027-ABP.

[67] D. Neuffer, *Part. Accel.* **14** (1983) 75.

[68] T. J. Roberts *et al., Conf. Proc.* **C0806233** (2008) WEPP120.

[69] R. C. Fernow, *eConf* **C990329** (1999) THP31.

[70] R. C. Fernow, PAC-2005-TPPP041.

[71] D. J. Summers *et al.,* arXiv:1504.03972.

[72] J. G. Acosta *et al.,* COOL-2015-MOPF07.

[73] S. J. Oliveros *et al.,* NAPAC-2016-MOB3CO04.

[74] S. Oliveros *et al.,* arXiv:1704.03891.

[75] S. J. Oliveros, FERMILAB-THESIS-2017-13.

[76] D. Neuffer, *AIP Conf. Proc.,* **441** (1998) 270.